

ALMA Imprint of Intergalactic Dark Structures in the Gravitational Lens SDP.81

Kaiki Taro Inoue^{1*}, Takeo Minezaki², Satoki Matsushita³, Masashi Chiba⁴

¹*Faculty of Science and Engineering, Kinki University, Higashi-Osaka, 577-8502, Japan*

²*Institute of Astronomy, School of Science, University of Tokyo, Mitaka, Tokyo 181-0015, Japan*

³*Academia Sinica Institute of Astronomy and Astrophysics, P.O. Box 23-141, Taipei 10617, Taiwan, Republic of China*

⁴*Astronomical Institute, Tohoku University, Aoba-ku, Sendai 980-8578, Japan*

24 July 2018

ABSTRACT

We present an analysis of the ALMA long baseline science verification data of the gravitational lens system SDP.81. We fit the positions of the brightest clumps at redshift $z = 3.042$ and a possible active galactic nucleus component of the lensing galaxy at redshift $z = 0.2999$ in the band 7 continuum image using a canonical lens model, a singular isothermal ellipsoid plus an external shear. Then, we measure the ratio of fluxes in some apertures at the source plane where the lensed images are inversely mapped. We find that the aperture flux ratios of band 7 continuum image are perturbed by 10–20 percent with a significance at $2\sigma \sim 3\sigma$ level. Moreover, we measure the astrometric shifts of multiply lensed images near the caustic using the CO(8–7) line. Using a lens model best-fitted to the band 7 continuum image, we reconstruct the source image of the CO(8–7) line by taking linear combination of inverted quadruply lensed images. At the 50th channel (rest-frame velocity 28.6 km s^{-1}) of the CO(8–7) line, we find an imprint of astrometric shifts of the order of 0.01 arcsec in the source image. Based on a semi-analytic calculation, we find that the observed anomalous flux ratios and the astrometric shifts can be explained by intergalactic dark structures in the line of sight. A compensated homogeneous spherical clump with a mean surface mass density of the order of $10^8 M_\odot h^{-1} \text{ arcsec}^{-2}$ can explain the observed anomaly and astrometric shifts simultaneously.

Key words: galaxies: formation - cosmology: theory - dark matter

1 INTRODUCTION

The nature of matter distribution on sub-galactic scales has been veiled in mystery. In comparison with the prediction from N -body simulations, the observed density profiles of dwarf galaxies are not cuspy but cored (Navarro et al. 1996; Moore et al. 1999; Swaters et al. 2003; Simon et al. 2005), the number of observed satellite galaxies in our Galaxy is too small (Klypin et al. 1999; Moore et al. 1999), and the observed circular velocities of most massive subhaloes in our Galaxy are too small (Boylan-Kolchin et al. 2011; Wang et al. 2012).

Gravitational lensing provides a powerful tool to measure the matter distribution on sub-galactic scales. It has been known that some quadruply lensed quasars show anomalies in the observed flux ratios of lensed images assuming that the gravitational potential of the lens is sufficiently smooth. Such a discrepancy is called the “anomalous

flux ratio” and has been considered as an imprint of cold dark matter subhaloes with a mass of $\sim 10^{8-9} M_\odot$ in lensing galaxies (Mao & Schneider 1998; Metcalf & Madau 2001; Chiba 2002; Dalal & Kochanek 2002; Keeton et al. 2003; Metcalf et al. 2004; Chiba et al. 2005; Inoue & Chiba 2005a,b; Sugai et al. 2007; McKean et al. 2007; More et al. 2009; Minezaki et al. 2009; Xu et al. 2009, 2010; Vegetti et al. 2012).

However, intergalactic haloes in the line of sight can act as perturbers as well (Chen et al. 2003; Metcalf 2005; Xu et al. 2012). Indeed, taking into account the astrometric shifts of lensed images, recent studies have shown that the observed anomalous flux ratios can be explained solely by intergalactic structures that consist of haloes, filaments and voids with a surface mass density $\sim 10^{7-8} M_\odot h^{-1} \text{ arcsec}^{-2}$ (Inoue & Takahashi 2012; Takahashi & Inoue 2014; Inoue 2015; Inoue et al. 2015) without considering subhaloes in the lens galaxy.

In order to determine the origin of flux-ratio anomalies, we need to measure the flux ratios and positions of

* E-mail: kinoue@phys.kindai.ac.jp

lensed images as precisely and as many as possible. If we find that the probability of having flux-ratio anomalies increases as a function of the source redshift, then it will be a strong indication that the anomaly is caused by the line-of-sight structures rather than subhaloes. For achieving this scientific goal, strongly lensed submillimetre galaxies (SMGs) are ideal targets as their redshifts are biased at $z=2-3$ (Simpson et al. 2014).

The lens system SDP.81, also known as H-ATLAS J090311.6+003906 is one of such systems. The source is an SMG at $z = 3.042$ (Negrello et al. 2010) and the primary lens is a massive elliptical galaxy at $z = 0.2999$ (Negrello et al. 2014). The property of the source has been extensively studied (Rybak et al. 2015a; Rybak et al. 2015b; Tamura et al. 2015; Hatsukade et al. 2015; Wong et al. 2015). However, we note that all of these models are based on smooth potentials without fully incorporating the small-scale structure of the lens system.

In this paper, we report our analysis of the ALMA long baseline science verification data of SDP.81 (used by the authors previously mentioned) to investigate possible gravitational perturbations by dark (sub-)structures along the line of sight to the lens system.

This paper is organized as follows. In section 2, we describe the data. In section 3, we explain the model of the primary lens and our method for reconstructing and modelling the data. In section 4, we present our results on the fitting of our model. In section 5, we show the semi-analytic estimate of perturbation by intergalactic dark structures and the analytic estimate of possible perturbation by a spherically symmetric homogeneous clump. In section 6, we conclude and discuss some relevant issues.

In what follows, we assume a cosmology with matter density $\Omega_{m,0} = 0.3134$, baryon density $\Omega_{b,0} = 0.0487$, a cosmological constant $\Omega_{\Lambda,0} = 0.6866$, a Hubble constant $H_0 = 67.3 \text{ km s}^{-1} \text{ Mpc}^{-1}$, a spectrum index $n_s = 0.9603$, and the root-mean-square (rms) amplitude of matter fluctuations at $8h^{-1} \text{ Mpc}$, $\sigma_8 = 0.8421$, which are obtained from the observed CMB (Planck+WMAP polarization; Planck Collaboration et al. (2014)). In plots of images, the horizontal and vertical coordinates correspond to R.A and Dec. in arcsec, respectively.

2 DATA

We used the ALMA science verification data on SDP.81 taken from the ALMA Science Portal (see ALMA Partnership et al. (2015b) for detail). SDP.81 was observed in 2014 October as part of the Long Baseline Campaign at band 4(151 GHz), 6(235 GHz) and 7(290 GHz). In addition to continuum, the bands 4, 6, and 7 data include lines of CO(5-4)(observed frequency=142.570 GHz), CO(8-7)(228.055 GHz), and CO(10-9)(285.004 GHz), respectively. We used the processed archival images of the band 6 and 7 continuums and the CO(8-7) line, whose calibration and imaging were carried out using the Common Astronomy Software Applications (CASA) (McMullin et al. 2007). The images were processed using the CLEAN algorithm with a *robust* = 1 weighting (Briggs weighting) of the visibilities. The CO data were binned spectrally into channels with 21.0 km s^{-1} wide. In this paper, we used the band 6 and 7 con-

tinuum images without *uv*-tapering and the CO(8-7) images with *uv*-tapering (1000k λ) to a resolution of ~ 170 mas in order to increase the signal-to-noise ratio on each pixel. In order to investigate astrometric shifts, we chose CO(8-7) images at channels 47 to 52 (rest-frame velocities from -34.4 km s^{-1} to 70.6 km s^{-1}). The pixel sizes are 0.005 and 0.02 arcsec, respectively. The semi-major and semi-minor axes and the position angles (PAs) of the synthesized beams are $31 \times 23 \text{ mas}$ (PA= 16°) and $169 \times 117 \text{ mas}$ (PA= 47°), respectively.

3 METHOD

3.1 Canonical Lens Model

As a canonical model of the unperturbed lensing galaxy, we adopt a singular isothermal ellipsoid (SIE) (Kormann et al. 1994), which has been widely used in lens modelling and has successfully reproduced many other lens systems (e.g., Keeton et al. (1998)). In order to fit the model, we used the relative positions of lensed quadruple images and the centroid of lensing galaxy obtained from CLEANed images. As is well known, the CLEAN algorithm is nonlinear and produces real-space images with non-trivial noise properties. As a result it is not possible to easily come up with a statistically well justified error when the lens modelling is done. In order to minimize this effect, we only used positions of brightest peaks with a signal-to-noise ratio $S/N \gtrsim 10$. The other fainter spots along the Einstein ring are more prone to such noises. The contribution from groups, clusters, and large-scale structures at angular scales larger than the Einstein angular radius of the primary lens was taken into account as an external shear (ES). The parameters of an SIE plus an ES (SIEES) model are the effective Einstein angular radius (the mass scale inside the critical curve) b^1 , the apparent ellipticity e of the lens and its position angle θ_e , the strength and the direction of the external shear (γ, θ_γ) , the lens position (x_G, y_G) , and the source position (x_s, y_s) . The angles θ_e and θ_γ are measured counter-clockwise from North.

In order to implement the simultaneous χ^2 fitting of the positions of the centroids of lensed images and the lensing galaxy, we used our developed code. We checked the accuracy of our code by comparing it with other numerical codes such as GRAVLENS². The obtained χ^2 values are consistent each other within a few percent.

3.2 Source Reconstruction

If a lens model is perfectly correct and observational noises are negligible, the source images that are inverted from multiple images should be all identical. However, in practical setting, they are different to some extent due to the error in the model, the noise and the finite resolution in the observed image. In order to reconstruct the brightness distribution of a source for a given lens model, we use linear combination of source images that are inverted from multiple images.

Let c_i 's and f_i 's ($i = 1, 2, \dots, N$) be arbitrary real

¹ We use the definition adopted in Kormann et al. (1994).

² See <http://redfive.rutgers.edu/~keeton/gravlens/>

functions that represent “weights” and surface brightness in the source plane corresponding to N -multiply lensed images. The true surface brightness f_{true} of a source can be estimated by a linear combination

$$f_{true} \sim f(\mathbf{r}; \mathbf{c}) \equiv \frac{\sum_{i=1}^N c_i(\mathbf{r}) f_i(\mathbf{r})}{\sum_{i=1}^N c_i(\mathbf{r})}, \quad (1)$$

where \mathbf{r} is the position in the proper coordinates in the source plane. In principle, the weight function c_i can be determined by changing weights at each pixel in the source plane. However, the degree of freedom of weights is N times larger than that of the f_{true} . Therefore, we have to put a certain prior on the weights. In what follows, we use the following two types of weighting scheme; the “uniform weight” (U-weight) in which $c_i \equiv 1$ and the “magnification weight” (M-weight) in which $c_i = \mu_i$ where μ_i is the magnification for the i -th lensed image. The uniform weight is preferable in the cases where the effect of astrometric shifts by subhaloes or intergalactic structures dominates over the observational noise effect. As this scheme puts the weight equally over the inverted images, the position errors for the best-fitted model with a smooth potential are minimized provided that the perturbation scale is sufficiently smaller than the Einstein radius of the primary lens. In contrast, the magnification weight is preferable in the cases where the observational noise effect dominates over the effect of perturbation. In fact, it corresponds to the inverse-variance weighted average if the observational noise in the image plane is homogeneous.

3.3 Modelling

In this analysis, we used only the positions of bright clumps that are not too close to the caustic and a possible active galactic nucleus (AGN) emission in the band 7 continuum image (ALMA Partnership et al. 2015b; Tamura et al. 2015) for modelling the unperturbed lens. Note that the angular resolution of the band 7 data is the highest in the data set. Our modelling procedure can be verified as follows. First, the expected change in the flux ratios are of the order of 10 percent (Inoue & Takahashi 2012). Therefore, it is difficult to measure such a tiny change with much fainter clumps in the observed arc. Second, bright clumps that are too close to the caustic are sensitive to astrometric shifts caused by subhaloes or intergalactic structures. Typical astrometric shifts due to subhaloes or intergalactic structures are of the order of 0.01 arcsec (Inoue & Takahashi 2012). These shifts yield significant changes in the fluxes of these clumps and consequently make a lens model with a smooth potential difficult to fit.

After a careful analysis of both the band 7 continuum (Fig. 1) and the CO(8-7) line images (Fig. 2), we found that the band 7 image can be well fitted by a fold-caustic lens with one set of quadruples (Aq1, Bq1, Cq1, Dq1) and two sets of doubles (Ad1, Ad2 and Dd1, Dd2) as demonstrated in Fig. 1. B and D have a positive parity and A and C have a negative parity. In order to fit the model, we used the positions of the brightest peaks of lensed images of these three sets (clumps) except for Aq1, which is difficult to identify.

As the signal to noise ratios of these clumps are $\gtrsim 10$ on each pixel, the errors in the relative positions of the clumps are expected to be much smaller than the band 7 beam size 23×31 mas. If the clump consists of a point source and

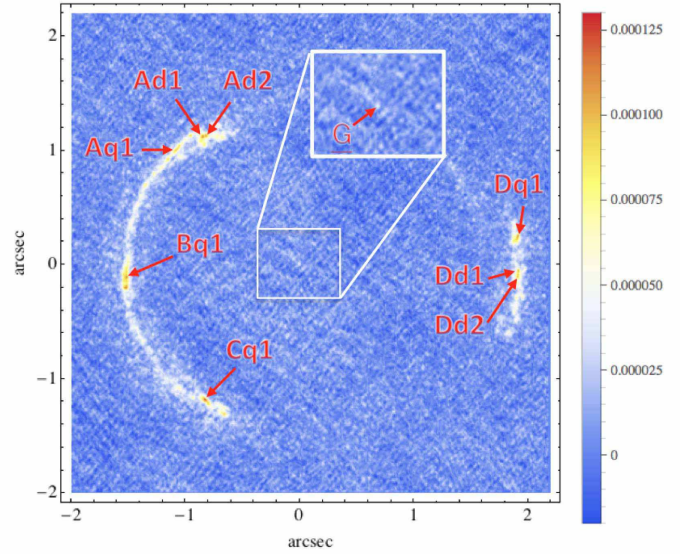


Figure 1. Band 7 continuum image of SDP.81. The unit is Jy per beam. The quadruply lensed clumps are Aq1, Bq1, Cq1, and Dq1. The doubly lensed “north” and “south” clumps are Ad1, Dd1 and Ad2, Dd2, respectively. G is a possible AGN emission.

the observational noise is dominated by thermal noise, we expect that the position measurement uncertainty for the peaks is given by

$$\Delta\theta \approx \left(\frac{4}{\pi}\right)^{1/4} \frac{1}{\sqrt{8 \ln 2}} \frac{\theta_{\text{beam}}}{SNR} \approx 0.451 \frac{\theta_{\text{beam}}}{SNR}, \quad (2)$$

where θ_{beam} is the synthesized beam size (measured in FWHM) and SNR is the signal-to-noise ratio (Reid et al. 1988; Reid & Honma 2014), which yields $\Delta\theta = 1 - 1.4 \text{ mas}^3$. In the model fitting, taking account of possible complex structures of the source within the beam, we used more conservative values for the position measurement uncertainty: the 1σ errors are $1/4$ of θ_{beam} , i.e., $6 \times 8 \text{ mas}$ with the same PA direction. We also used the position of the centroid of image G, a possible emitting region from the AGN in the lensing galaxy. G was identified by overlaying the continuum image in the band 6 with that in the band 7. The distance between the centroids of G in the band 6 and 7 is 0.02 arcsec. Therefore, we assumed that the 1σ error in the position of the centroid of G is 0.02 arcsec, which is similar to the beam size θ_{beam} .

In what follows, we call a quadruply lensed image that belongs to the inverted image of the region inside the caustic and contains Aq1, image A. Images B, C, and D are defined in a similar manner. The centre (0,0) of the coordinates in the image plane (x, y) is set at the centroid of image G.

³ Note that the nominal astrometric accuracy from the ALMA Long Baseline Campaign tests is an rms positional error of 1.5 mas, which is for an average calibrator-target separation of 6 deg with an observing period of one hour with a maximum baseline of 12 km (ALMA Partnership et al. 2015a).

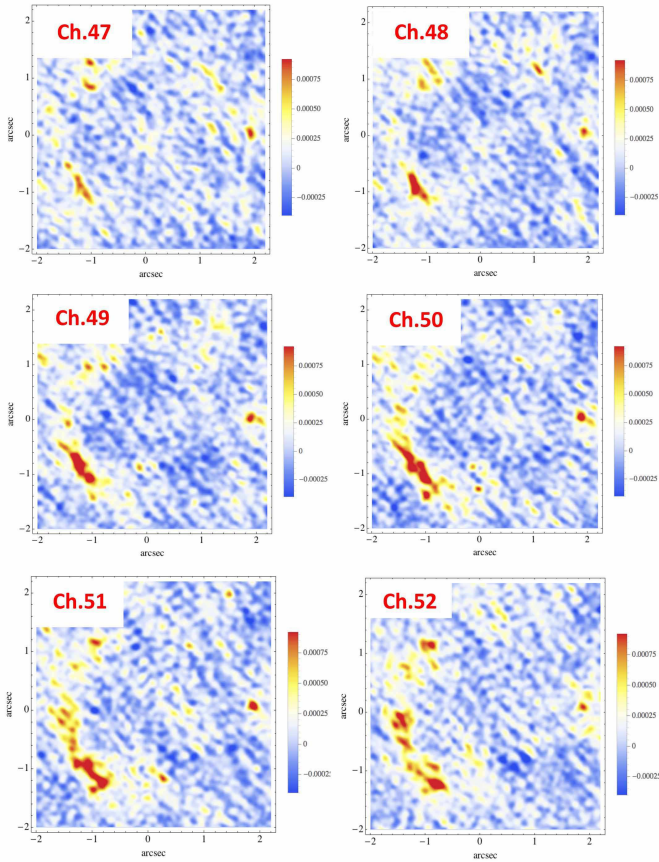


Figure 2. CO(8-7) line images of SDP.81 at channels 47 to 52 (rest-frame velocities from -34.4 km s^{-1} to 70.6 km s^{-1}). The unit is Jy per beam.

4 RESULT

4.1 Best-fitted Model

The parameters of the best-fitted SIEES model based on the band 7 continuum image is shown in Table 1. The degree of freedom for the observables is 16 and that for the model parameters is 13. Therefore, the reduced χ^2 ($= \chi^2/\text{dof}$) is $0.647/(16-13) = 0.22$. The mean distance between the position of the best-fitted and observed lensed images was found to be 0.0014 arcsec. This over-fitting may imply that the estimate of position accuracy ($=\text{beam size}/4$) in our analysis is a conservative one and astrometric shifts by perturbers are sufficiently small for the quadruples of q1.

The lensed images, the caustic and critical curve, and the reconstructed source images for the best-fitted model are shown in Figs. 3, 4, and 5, respectively. The 1σ uncertainty in the model parameters are obtained by finding a range of each parameter that gives the reduced χ^2 less than 1.

Our result is in agreement with the parameters obtained by Rybak et al. (2015a), Dye et al. (2015) and Tamura et al. (2015). Though our best-fitted parameters are slightly deviated from their values, the differences fall within 1σ - 2σ errors in our analysis.

Apart from minor differences in the lens model (power-law index, core, etc.), the slight differences in the best-fitted

parameters mainly come from degeneracy between ellipticity e and external shear γ : the sum of e and γ is nearly constant. In order to investigate this effect, we searched for another set of parameters that are much closer to those in Dye et al. (2015) by changing e and γ . Then we found a set of “concordant” model parameters (Table 2). The differences between the “concordant” parameters and those in Dye et al. (2015), which uses a semi-linear inversion method, fall within 1σ errors in their data. The reduced χ^2 ($= \chi^2/\text{dof}$) for the “concordant” model is $1.51/(16-13) = 0.50$.

Moreover, we also computed parameters for which the orientations of the SIE and an external shear θ_e, θ_γ coincide with the values in Dye et al. (2015) as well as e and γ for checking consistency (Table 3). We fixed the power-law index $\alpha = 2$ of the gravitational potential of the primary lens, and optimized the parameters of b and the source positions (x_s, y_s) of the three clumps. The reduced χ^2 ($= \chi^2/\text{dof}$) for the model based on a semi-linear inversion method is $5.18/(16-13) = 1.7$. Thus, our best-fitted values are slightly deviated from those in Dye et al. (2015) but the difference falls within 2σ .

4.2 Flux in Aperture

If a lensed image is significantly distorted, it is difficult to correctly measure the fluxes of an identical component of the source in the image plane. Therefore, we measure the relative aperture fluxes of quadruply lensed images at the *source plane*. If the model is perfect and the noise is negligible, then the inverted aperture flux ratios should be equal to 1. Any deviation from 1 indicates anomaly in the flux ratio, unless it is caused by observational errors.

In order to invert the observed image in the image plane back to the source plane, we use three models, namely the “best-fitted”, the most probable model, the “concordant”, which is concordant with models in literature, and the “semi-linear inversion” model introduced in Dye et al. (2015). In order to reduce the systematic effect of beam smoothing, the size of an aperture radius is taken to be sufficiently larger than the inverted beam size while most of the flux is contained inside the choice of aperture (see Fig. 6).

As shown in Fig. 4, the quadruply lensed source consists of two “north” and “south” extended components. A component q1 that yield quadruples in the source plane is at the right end of the “south” region which may have more complex structures. The centre of apertures was chosen so that these components are contained within a radius of 0.04 arcsec. As the maximum linear sizes of the inverted beams are less than ~ 0.04 arcsec, an aperture radius of > 0.04 arcsec is necessary to reduce the beam smoothing effect.

To estimate the significance of deviation in the ratios of fluxes in aperture, we have carried out Monte Carlo simulations using subsamples in the data. First, we randomly selected 100 points within a ring region with an angular distance R from the centre of the lens satisfying $3.5 < R < 4.3$ arcsec. The region with $R < 3.5$ arcsec was not used because we observed a systematic deviation from zero in the fluxes. It may be caused by either a part of broad Einstein ring of lensed image or possible foreground emission from the lensing galaxy. Thus the observed fluxes in this ring region are expected to be dominated by observational noises. Then for each point, we made a translation of the image

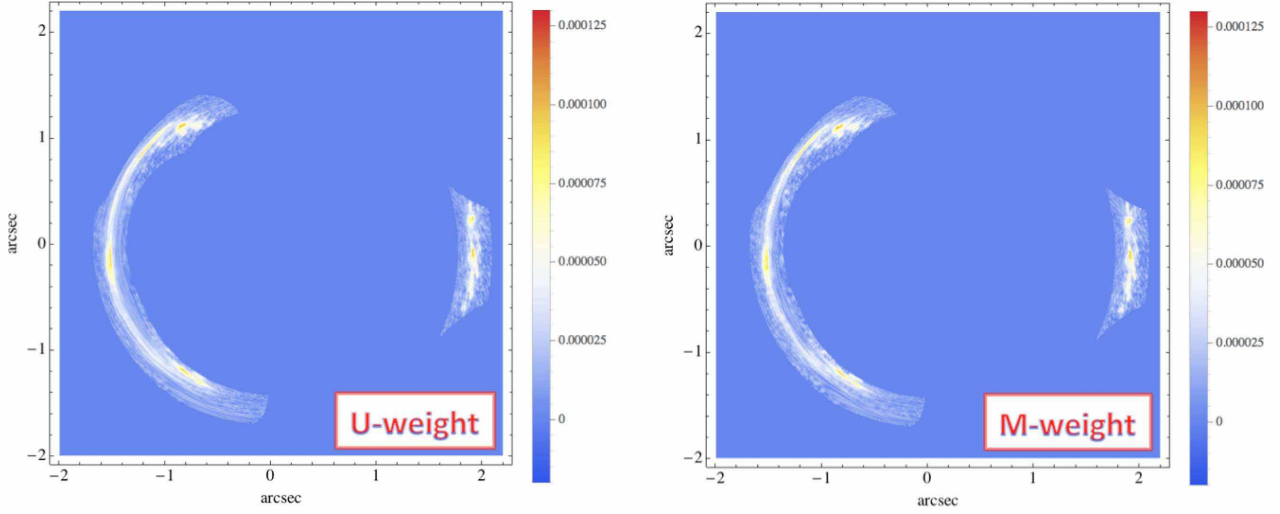


Figure 3. Modelled surface brightness distribution in the image plane for the uniform weight (left) and the magnification weight (right) for the best-fitted SIEES model based on the band 7 continuum image. The unit is Jy per beam.

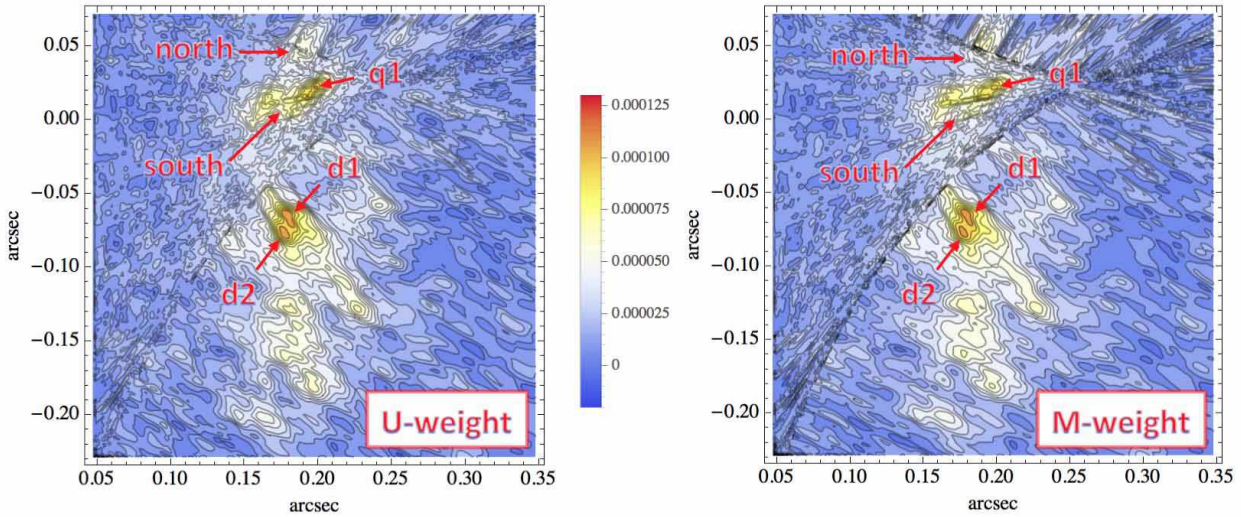


Figure 4. Modelled surface brightness distribution in the source plane for the uniform weight (left) and the magnification weight (right) for the best-fitted SIEES model based on the band 7 continuum image. The unit is Jy per beam.

Table 1. Best-fitted Model Parameters

χ^2/dof	(x_G, y_G) (arcsec)	b (arcsec)	e	θ_e (deg)	γ	θ_γ (deg)
0.647/3	(-0.007, -0.017)	$1.605^{+0.030}_{-0.004}$	$0.17^{+0.17}_{-0.09}$	25^{+44}_{-14}	$0.057^{+0.038}_{-0.039}$	-10^{+10}_{-0}
	(x_s, y_s) (arcsec) for q1	(x_s, y_s) (arcsec) for d1	(x_s, y_s) (arcsec) for d2			
	(0.1978, 0.0215)	(0.1783, -0.0645)	(0.1781, -0.0780)			

of the diamond-shaped region inside the caustic for each multiple image separately so that the lensed images of $q1$ coincide with the point. Finally, we inverted the observed band 7 image within the translated region back to the source plane and computed the fluxes in circles with aperture ra-

dius 0.04, 0.05, 0.06 arcsec to obtain observational errors in the source plane.

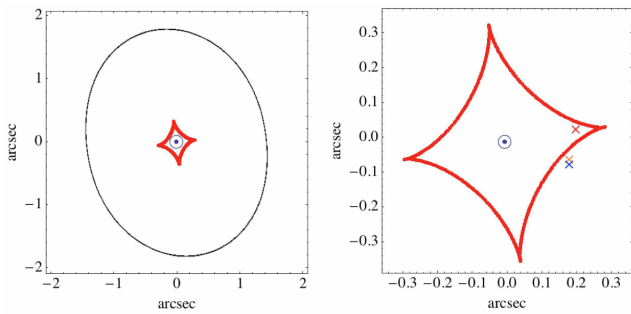
The leak of flux outside or inside aperture can be a source of systematics. In order to estimate the effect, we carried out a hypothetical observation in which the source image is identical to the one reconstructed from image A

Table 2. Concordant Model Parameters

χ^2/dof	(x_G, y_G) (arcsec)	b (arcsec)	e	θ_e (deg)	γ	θ_γ (deg)
1.51/3	(−0.024, −0.005)	1.609	0.20	16	0.041	−8
(x_s, y_s) (arcsec) for q1 (x_s, y_s) (arcsec) for d1 (x_s, y_s) (arcsec) for d2						
(0.1961, 0.0312) (0.1862, −0.0579) (0.1860, −0.0722)						

Table 3. Model Parameters Based on Semi-linear Inversion (Dye et al. 2015)

χ^2/dof	(x_G, y_G) (arcsec)	b (arcsec)	e	θ_e (deg)	γ	θ_γ (deg)
5.18/3	(−0.033, 0.005)	1.606	0.20	13	0.040	−4
(x_s, y_s) (arcsec) for q1 (x_s, y_s) (arcsec) for d1 (x_s, y_s) (arcsec) for d2						
(0.1904, 0.0375) (0.1873, −0.0515) (0.1872, −0.0664)						

**Figure 5.** Critical curve (black) and caustic (red) for the best-fitted SIEES model based on the band 7 continuum image. The centre of the coordinates is at image G. The circled dot indicates the position of an SIE and crosses represent the positions of bright clumps.

and image D using the magnification weight. Then we convolved the obtained image with an elliptic Gaussian beam that corresponds to the one in the band 7 continuum image and computed aperture fluxes. We have found that the errors in the aperture flux ratios are less than 4 percent. As the reconstructed lensed images of the tentative source image are smoothed twice, the actual size of the source clumps are expected to be much smaller. Thus our test of systematics gives an upper limit on the error caused by the beam shape.

In Table 4, we show our results of the aperture fluxes in the band 7 image. In this table, B/A, C/A and D/A represent aperture flux ratios of B to A, C to A, and D to A and “deviation” is defined as $1 - (\text{flux ratio})$ divided by 1σ error obtained from the randomly chosen 100 samples. Note that the error caused by the beam shape is not taken into account here. In the best-fitted model, the aperture fluxes of images B and C are deviated from 1 at $\sim 3\sigma$ level whereas image D is equal to 1 within an error. In the concordant model, the significance of anomaly in images B and C is lowered to $\sim 2\sigma$, and image D is consistent with being 1. In

the “semi-linear inversion” model, however, the significance of anomaly in C is further lowered by $\sim 1\sigma$ but that in B does not change.

In the best-fitted model, the magnifications of the bright clump q1 at images A and D are 6.87 and 3.92 and those at images B and C are 21.9 and 18.2. As the perturbation of magnification divided by the unperturbed magnification is proportional to the unperturbed magnification (Inoue & Takahashi 2012), the perturbation for image A is 2-3 times smaller than those for images B and C. Perturbation for image D is much smaller. Thus, the expected perturbation due to line-of-sight dark structures is much larger in images B and C than images A and D. Therefore, the observed anomalous result for only images B and C is consistent with the interpretation that they are perturbed by either subhaloes or the line-of-sight structures provided that the non-perturbed smooth gravitational potential is described by that of an SIE and an ES.

For the band 6 image, it turned out that the aperture flux-ratios B/A and C/A are ~ 0.9 with slightly larger errors. Thus, we were not able to find any anomalous features in the aperture flux ratios in the band 6 image. However, the obtained result is consistent with that for the band 7 image within 1σ .

The elongation of the inverted beams in the source plane may cause some errors in estimating the aperture flux ratios. However, the deviation from 1 for D/A is less than 5 percent. Therefore, we expect that the beam effect is less than 5 percent provided that image A and image D are not perturbed at all. This is consistent with the analysis using a hypothetical observation that we have mentioned. Thus, it does not change our conclusion that the aperture flux-ratios show anomaly at 2σ - 3σ level.

A strange feature is observed in B/A. If B is perturbed by a clump, B should be *magnified* since B has a positive parity (Inoue & Chiba 2005b; Inoue & Takahashi 2012). However, our result indicates that image B is *demagnified* in comparison with the prediction of a best-fitted model with a smooth potential. The feature may be a problem if one

tries to explain the anomaly by putting a single subhalo in the lensing galaxy. However, it can be easily explained by a line-of-sight dark structure with a negative density region, which we discuss in the next section.

4.3 Astrometric Shift

The perturbation of gravitational acceleration due to dark structures also causes astrometric shifts of lensed images. This effect is usually difficult to observe as the observable signal of shifts is quite subtle. However, if the source is very close to caustics, the effect becomes significant as the magnification can be changed drastically by such shifts. ALMA is an ideal tool for finding such an effect.

In order to find astrometric shifts, we analysed the inverted CO(8-7) line data of SDP.81 using the best-fitted lens model based on the band 7 data. As shown in Figs 7 and 8, a discontinuous change in the surface brightness across the caustic is observed at Ch.50. This suggests that a bright clump is crossing the caustic at the Ch.50. In order to look into the crossing, we plot the sum of A and D images in Fig. 9. One can clearly see that a bright clump centred at approximately (0.18, -0.02) in the source plane is crossing the caustic, which yields elongation of the inverted image along the caustic. However, it turned out that the elongation is asymmetric around a bright clump. In order to show this feature, we plot the difference in the surface brightness between the inverted image reconstructed from B and C images (B+C) and that from of A and D images (A+D) in Fig. 9. One can see a distinctive feature at the region centred at $\sim (0.19, -0.02)$ in the source plane. The amplitude of the feature is $\gtrsim 3\sigma$. However, no distinctive feature is observed at $\sim (0.16, -0.04)$. This is an asymmetric feature around the brightest clump: the surface brightness changes discontinuously at the caustic.

This feature suggests astrometric shifts of the order of 0.01 arcsec perpendicular to the caustic for B and C images assuming that A and D images are not perturbed at all. As the signal-to-noise ratio of the brightest clump near the caustic is found to be ~ 8 , equation (2) gives the expected positional uncertainty ~ 0.01 arcsec. Therefore, the observed feature is much larger than the uncertainty. If this is the case, B and C images might have been perturbed by some dark structures in the line-of-sight. The observed anomalous feature in the aperture flux-ratios in band 7 data supports this interpretation.

5 PERTURBATION BY INTERGALACTIC STRUCTURES

In this section, we briefly introduce the semi-analytic method for estimating the perturbative effect on the magnification of lensed images caused by intergalactic structures in the line of sight. For detail, see Inoue & Takahashi (2012); Takahashi & Inoue (2014).

5.1 Semi-analytic Estimate

We introduce a statistic η adopted in (Inoue & Takahashi 2012) to measure the perturbation of magnification in strong lens systems. Let us consider a lens system with N -multiple

images of a point source. The magnification contrast of the image "i" is defined as $\delta_i^\mu \equiv \delta\mu_i/\mu_i$, where μ_i is the magnification of the image "i" expected in the best-fitted model with a smooth gravitational potential and $\delta\mu_i$ is the perturbation of μ_i . If the parity of an image is positive (negative), then the curvature of the arrival time surface at the image position is positive (negative). Therefore, the surface is locally minimum or maximum (saddle) at the point. In what follows, we ignore images that correspond to maxima, since they are typically extremely faint.

In terms of δ_i^μ 's, the magnification perturbation η is defined as

$$\eta \equiv \left[\frac{1}{2N_{\text{pair}}} \sum_{i \neq j} [\delta_i^\mu(\text{minimum}) - \delta_j^\mu(\text{saddle})]^2 \right]^{1/2}, \quad (3)$$

where $\delta_i^\mu(\text{minimum})$ and $\delta_j^\mu(\text{saddle})$ are the magnification contrasts of the minimum image and saddle image, respectively, and N_{pair} is the total number of pairs of a saddle and a minimum images. The summation is performed over all the pairs. Roughly speaking, η is equal to the mean value averaged over the all multiple images if correlations of flux perturbation between the lensed images are not taken into account. In SDP.81, there are two minima B and D and two saddles A and C. Then, we have

$$\eta \equiv \left[\frac{1}{8} \left[(\delta_B^\mu - \delta_A^\mu)^2 + (\delta_D^\mu - \delta_C^\mu)^2 + (\delta_B^\mu - \delta_C^\mu)^2 + (\delta_D^\mu - \delta_A^\mu)^2 \right] \right]^{1/2}. \quad (4)$$

Up to the linear order in δ_i^μ , in terms of observed fluxes $\mu_A, \mu_B, \mu_C, \mu_D$ and estimated unperturbed fluxes $\mu_{A0}, \mu_{B0}, \mu_{C0}, \mu_{D0}$, the estimator of η is approximately given by

$$\hat{\eta} \approx \left[\frac{1}{8} \left[\left(\frac{\mu_B \mu_{A0}}{\mu_A \mu_{B0}} - 1 \right)^2 + \left(\frac{\mu_D \mu_{A0}}{\mu_A \mu_{D0}} - 1 \right)^2 + \left(\frac{\mu_B \mu_{C0}}{\mu_C \mu_{B0}} - 1 \right)^2 + \left(\frac{\mu_D \mu_{C0}}{\mu_C \mu_{D0}} - 1 \right)^2 \right] \right]^{1/2}. \quad (5)$$

For extended sources, we need to use aperture fluxes defined at the source plane. If the source size is sufficiently small in comparison with the Einstein radius of the primary lens, and distance between the source and the caustic is sufficiently large, then we can neglect the differential magnification effect. In that case, in terms of estimated unperturbed aperture fluxes $m_{A0}, m_{B0}, m_{C0}, m_{D0}$ at the source plane, the estimator of η is approximately given by

$$\hat{\eta} \approx \left[\frac{1}{8} \left[\left(\frac{m_{B0}}{m_{A0}} - 1 \right)^2 + \left(\frac{m_{D0}}{m_{A0}} - 1 \right)^2 + \left(\frac{m_{B0}}{m_{C0}} - 1 \right)^2 + \left(\frac{m_{D0}}{m_{C0}} - 1 \right)^2 \right] \right]^{1/2}. \quad (6)$$

In order to estimate the magnification perturbation η theoretically, we use a formalism based on the non-linear power spectrum of density perturbation.

First, we divide density fluctuations that cause lensing into two parts: strong lens and weak lens components. The strong lens component corresponds to the primary lens and

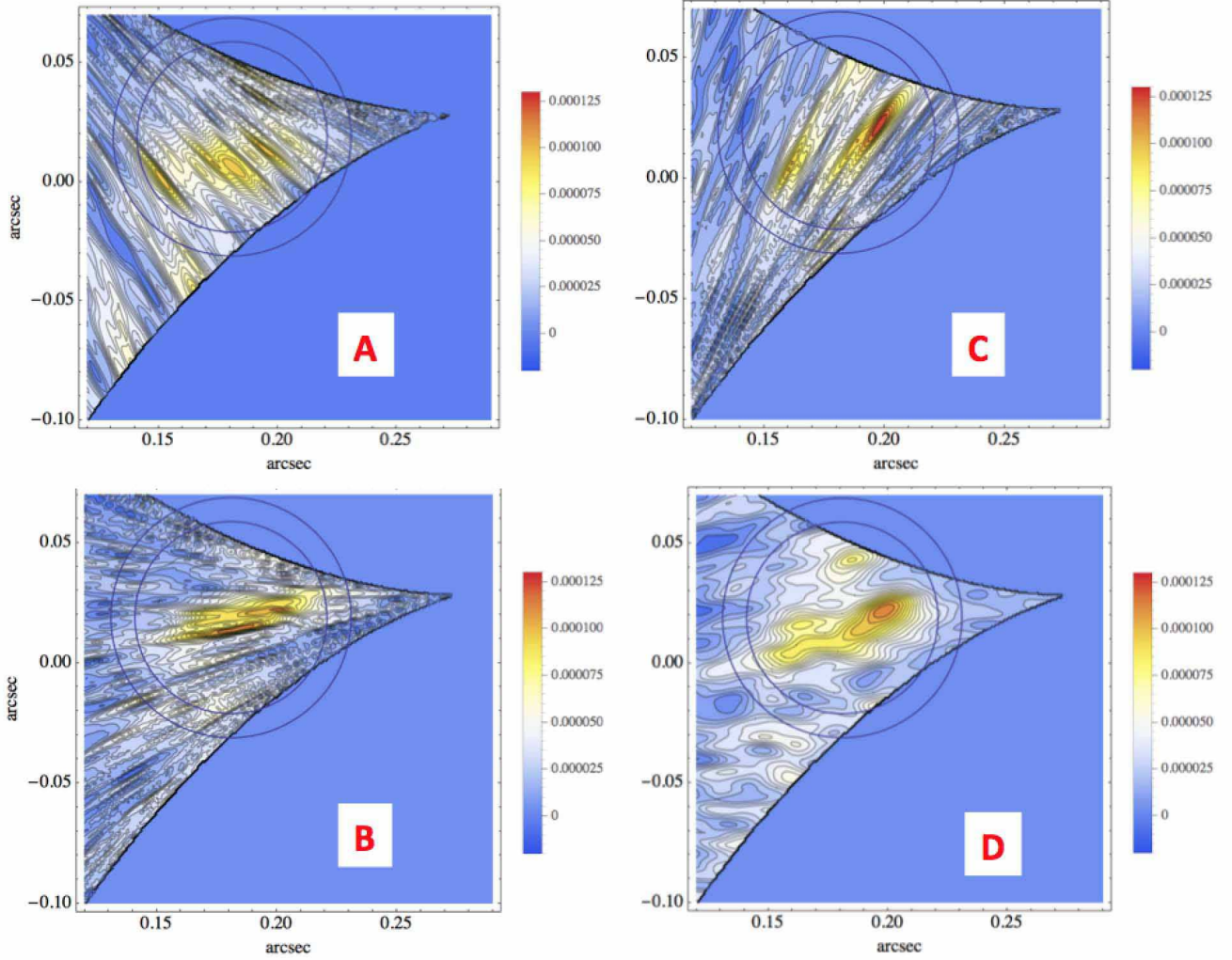


Figure 6. Inverted quadruple images of band 7 data using a best-fitted SIEES model. The unit is Jy per beam. Blue circles denote apertures with a radius 0.04 and 0.05 arcsec. The centre of the apertures is (0.1809, 0.01882).

the line-of-sight density fluctuations whose angular scales are comparable to or larger than the mean separation θ_0 between the centre of the primary lens and multiple images. In our case, it corresponds to a best-fitted SIEES. The weak lens component corresponds to the remaining line-of-sight density fluctuations whose angular scales are smaller than the mean separation, and which causes astrometric shifts and perturbation of fluxes.

Secondly, we estimate the observed strength of weak lens component due to line-of-sight structures using the residual difference ϵ in the best-fitted positions of multiple images. The difference gives an upper limit of possible contribution from line-of-sight structures. Since the contribution to the magnification perturbation decreases as the comoving scale of the density fluctuations, we assume that the fluctuations with angular scales just below θ_0 are mostly affected. Thus, from two physical scales θ_0 and ϵ , the second moment of η can be estimated. In the Fourier space, these effects can be taken into account by considering a filtering function $W(k)$ to the non-linear power spectrum $P(k)$ obtained from N -body simulations.

For the bright clump q1 in the band 7 data, the mean

separation between the center of the lens and lensed images that correspond to the bright component q1 is 1.64 arcsec, and the mean of ϵ is 1.4 mas. This suggests that the actual position uncertainty is much smaller than the value we assumed. Using so called the “constant shift” filtering function $W_{CS}(k)$ (Takahashi & Inoue 2014), the square-root of the second moment of η , $\langle \eta^2 \rangle^{1/2} = 0.135$ for 4 images, Aq1, Bq1, Cq1, Dq1 has been obtained. The corresponding probability distribution function $p(\eta)$ with the theoretically obtained second moment can be calculated using a fitting formula (Takahashi & Inoue 2014) that has been obtained from N -body and ray-tracing simulations that can resolve haloes with a mass of $\sim 10^5 M_\odot$ (for detail, see section 3 in (Takahashi & Inoue 2014)).

As shown in Fig. 10, $p(\eta)$ takes its peak at $\eta = 0.065$. One can see that the observed $\hat{\eta}$ shown in vertical lines (red and orange) with 1σ observational uncertainty (grey region) agrees with the prediction. The most probable values are close to the peak. Thus the observed anomalous aperture flux ratios in SDP.81 can be explained by the line-of-sight structures.

Table 4. Flux Ratios in Band 7

		aperture(arcsec)	$\hat{\eta}(1\sigma)$	B/A	C/A	D/A
best-fitted	0.06	0.092(0.031)	ratio	0.820	0.801	0.945
			error	0.062	0.060	0.073
			deviation	2.9	3.4	0.8
	0.05	0.092(0.031)	ratio	0.829	0.815	0.973
			error	0.058	0.058	0.072
			deviation	2.9	3.2	0.4
	0.04	0.097(0.030)	ratio	0.819	0.825	0.996
			error	0.055	0.057	0.071
			deviation	3.3	3.0	0.1
<hr/>						
		aperture(arcsec)	$\hat{\eta}(1\sigma)$	B/A	C/A	D/A
concordant	0.06	0.069(0.031)	ratio	0.857	0.868	0.982
			error	0.064	0.063	0.076
			deviation	2.2	2.1	0.2
	0.05	0.069(0.029)	ratio	0.857	0.877	0.991
			error	0.059	0.060	0.073
			deviation	2.4	2.0	0.1
	0.04	0.073(0.025)	ratio	0.846	0.893	1.008
			error	0.055	0.059	0.069
			deviation	2.8	1.8	0.1
<hr/>						
		aperture(arcsec)	$\hat{\eta}(1\sigma)$	B/A	C/A	D/A
semi-linear inversion (Dye et al. 2015)	0.06	0.061(0.032)	ratio	0.868	0.919	1.01
			error	0.068	0.068	0.080
			deviation	2.0	1.2	0.1
	0.05	0.067(0.030)	ratio	0.856	0.913	1.01
			error	0.062	0.065	0.076
			deviation	2.3	1.3	0.1
	0.04	0.080(0.028)	ratio	0.843	0.927	1.05
			error	0.057	0.063	0.072
			deviation	2.8	1.2	0.6

5.2 Homogeneous Spherical Clump

As a simple model of a perturber in the line of sight, we consider a homogeneous spherical dark clump that is compensated in mass. We assume that it has a positive uniform density ρ_+ inside radius R_+ and a negative uniform density ρ_- at $R_+ < R < R_-$, where R denotes the proper distance from the centre of a clump. At $R > R_-$, the density is vanishing, i.e., $\rho = 0$. The total mass at $R < R_+$ is $M = 4\pi\rho_+R_+^3/3$. Then, the X -component of the deflection angle $\hat{\alpha}_c$ at $\mathbf{R}_\perp = (X, Y = 0)$ in the lens plane is (Amendola et al. 1999),

$$\hat{\alpha}_c = b_c \times \begin{cases} 0, & R_- \leq |\mathbf{R}_\perp| \\ \tilde{X}^{-1}(\tilde{d}^3 + 3\tilde{d}^2 + 3\tilde{d})^{-1} \\ \times [(1 + \tilde{d})^2 - \tilde{X}^2]^{3/2}, & R_+ < |\mathbf{R}_\perp| < R_- \\ \tilde{X}^{-1}(\tilde{d}^3 + 3\tilde{d}^2 + 3\tilde{d})^{-1} \\ \times [(1 + \tilde{d})^2 - \tilde{X}^2]^{3/2} \\ - (1 + \tilde{d})^3(1 - \tilde{X}^2)^{3/2}, & 0 \leq |\mathbf{R}_\perp| < R_+, \end{cases} \quad (7)$$

where $\tilde{X} \equiv X/R_+$, $\tilde{d} \equiv R_-/R_+ - 1$, and b_c describes the mass scale, which is given by

$$b_c \equiv \frac{4GM}{c^2 R_+} = \frac{16\pi G R_c^2 \rho_+}{3c^2}. \quad (8)$$

The Y -component of $\hat{\alpha}_c$ is zero for $Y = 0$. For $Y \neq 0$, a rotation of coordinates by an angle $\phi = \tan^{-1}(Y/X)$ gives the deflection angle $\hat{\alpha}_c = (\hat{\alpha}_c, 0)$ as the clump is spherically symmetric. The reduced deflection angle $\hat{\alpha}_c$ is a function of \tilde{X} .

Thus, the parameters of a spherically symmetric compensated homogeneous clump is the mass scale b_c , the width of the shell \tilde{d} and the proper radius of the positive density region R_+ . b_c represents the maximum possible astrometric shift. The reduced deflection angle $\hat{\alpha}_c$ vanishes at the centre of a clump and takes its peak at $R = R_+$. For convenience, we choose the angular radius θ_+ of the positive density region as the parameter instead of R_+ . In terms of the angular diameter radius D of the clump, the angular radius is given

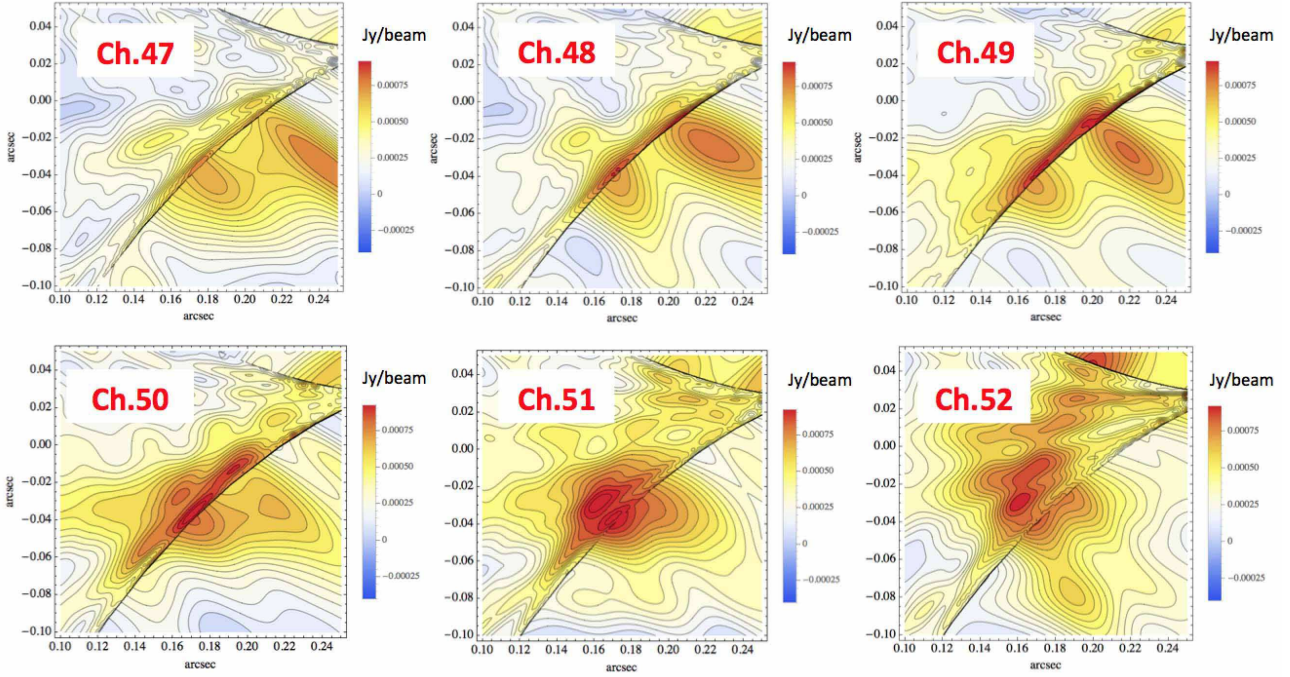


Figure 7. Reconstructed images (uniform weight) of the CO(8-7) data (Ch.47 to Ch.52) using the best-fitted SIEES model.

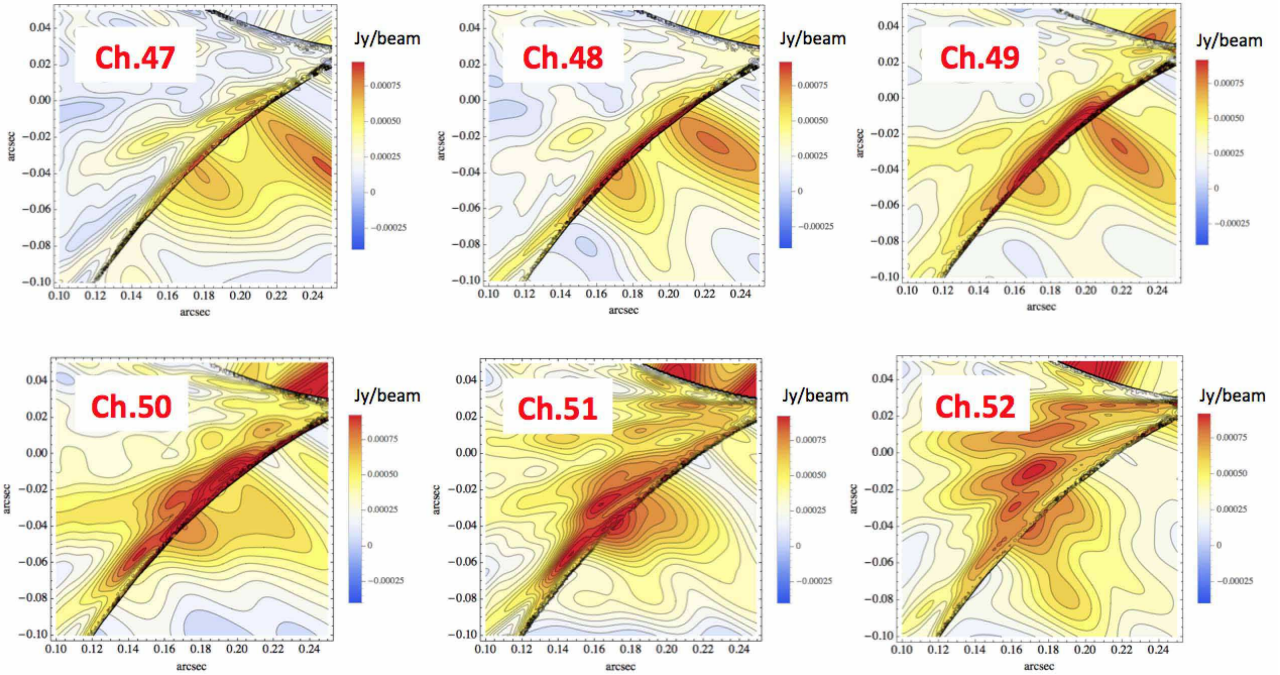


Figure 8. Reconstructed images (magnification weight) of the CO(8-7) data (Ch.47 to Ch.52) using the best-fitted SIEES model.

by $R_+ = D\theta_+$. The position of the centre of a clump in the image plane is denoted by (x_c, y_c) .

We study a toy model that consists of the best-fitted SIEES plus a homogeneous compensated spherical dark clump. In order to explain the observed anomalous flux ratios in the band 7 data and possible astrometric shifts in the CO(8-7) data, we put a spherical clump centred at image Cq1 in the band 7 data in the lens plane. After some trial

and errors, we found a set of parameters that can explain the both anomalous features (Table 5). The convergences of the clump at the positive and negative density regions are $\kappa = 0.014 \pm 0.014$ and $\kappa = -0.015 \pm 0.0075$, respectively (see Fig. 11). The mass inside $R_+ = 3.47\text{kpc}h^{-1}$ is $2.66 \times 10^9 M_\odot h^{-1}$ and the mean surface mass density inside R_+ is $6.76 \times 10^8 M_\odot h^{-1} \text{arcsec}^{-2}$. Because the gravitational

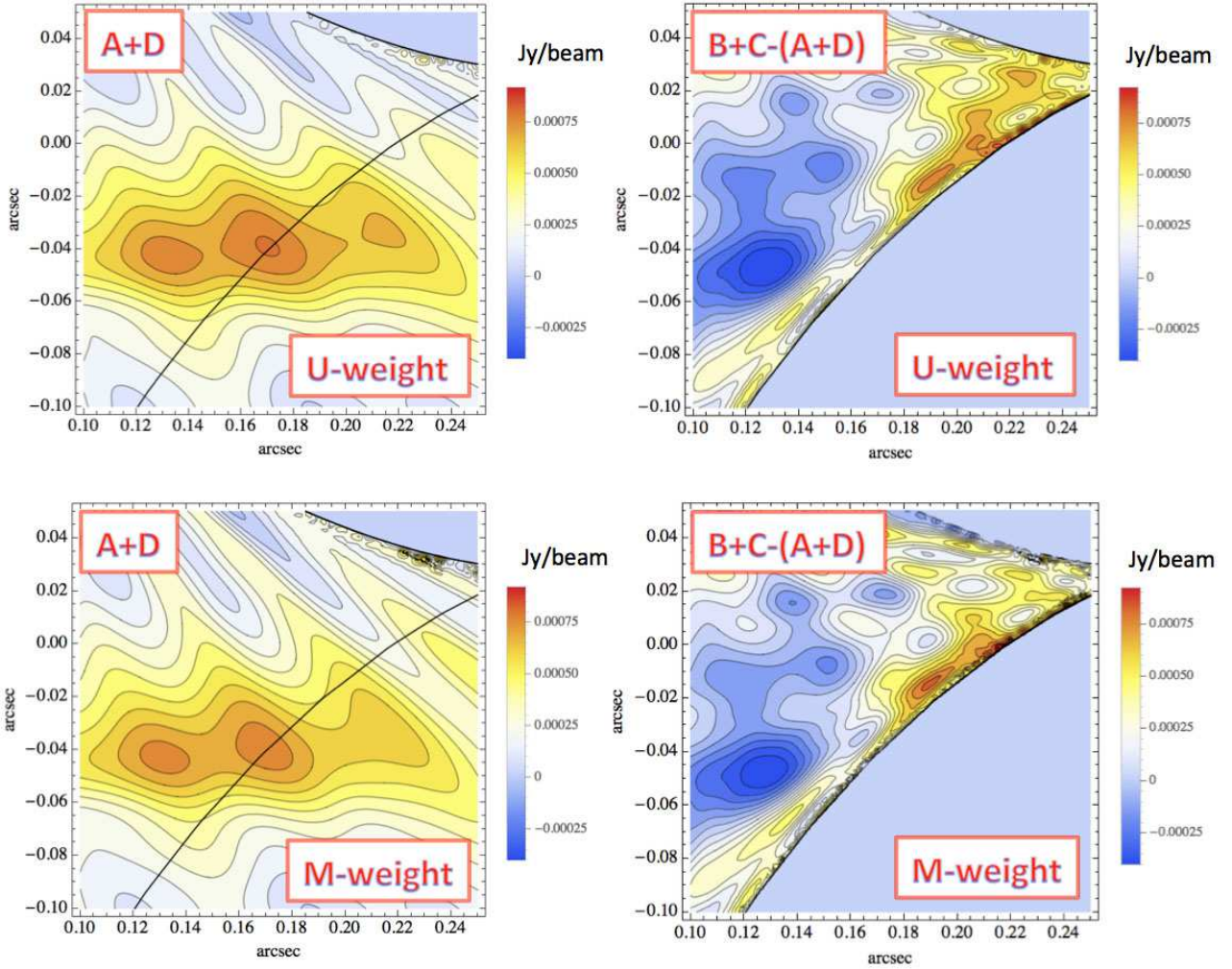


Figure 9. Reconstructed images of the CO(87) Ch.50 data for the best-fitted SIEES model: image reconstructed from A and D images (left) and the difference between an image reconstructed from B and C images and that reconstructed from A and D images (right).

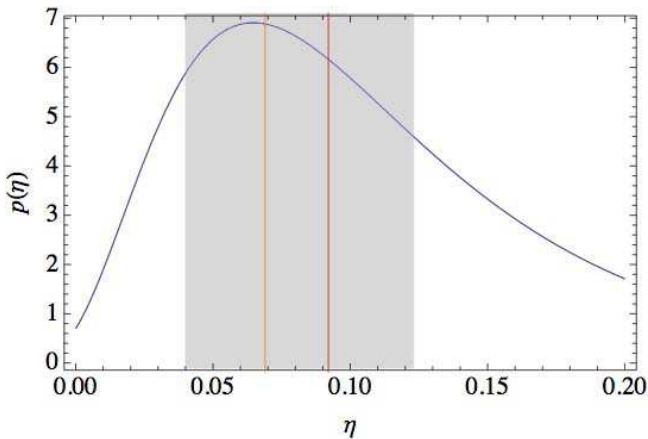


Figure 10. Theoretical and observed magnification perturbation η . The blue curve corresponds to the probability distribution function of η and the red and orange vertical lines correspond to the estimators $\hat{\eta}$ for the best-fitted and concordant lens models with aperture equal to 0.05 arcsec. The grey region shows 1σ uncertainties due to observational noises in the both lens models.

potential of a compensated clump vanishes at $R > R_-$, the effect on image A and image D is significantly small.

We also checked the expected amplitude of convergence perturbation due to line-of-sight dark structures using the semi-analytic method formulated in the Fourier space (Inoue & Takahashi 2012). Assuming that the maximum wavelength of the perturbation is given by four times the radius of a clump θ_+ , we found that the standard deviation is $\sqrt{\langle \kappa^2 \rangle} = 0.020$. Thus, the expected amplitude agrees with the convergence perturbation due to the clump we have considered.

In a similar manner described in section 4.2, we measured the inverted aperture flux ratios in the band 7 based on the best-fitted or concordant model with the clump. As shown in Table 5.2, the aperture flux ratios are consistent with being equal to 1 at the $0.5\sigma - 1.5\sigma$ level. Comparing with the result in Table 4.2, one can see that the positive density region within the clump induces a decrease in the inverted flux of image C in the band 7, which has a negative parity and the surrounding negative density shell also induces a decrease in that of image B in the band 7, which has a positive parity. Such a decrease cannot be expected for ob-

jects with a positive density provided that the unperturbed model has a smooth potential and the first spatial derivatives of the convergence, shear and magnification at the perturbed point are sufficiently small (Inoue & Takahashi 2012; Takahashi & Inoue 2014). If one considers the effect of astrometric shifts, demagnification may be explained by shifting the image B towards the opposite direction to the nearest cusp in the source plane. However, if one imposes an accuracy of ~ 0.001 arcsec in the position of q1, we find that the flux change would be just a few percent, which is not sufficient for explaining the systematic decrease of ~ 20 percent.

In Fig. 12, we plot the surface brightness profiles of the inverted quadruple images of the band 7 data in the perturbed model. The changes in the aperture fluxes in images B and C can be also explained by the fields of astrometric shift of the order of 0.01 arcsec due to a clump (Fig. 13).

The difference between the inverted image reconstructed from B and C images (B+C) and that reconstructed from A and D images (A+D) in the CO(8-7) 50th channel data has become small (Fig. 14) due to astrometric shifts of the order of 0.01 arcsec in the direction perpendicular to the caustic (Fig. 13). As one can see in Fig. 15, the reconstructed source images in the CO(8-7) data in the neighbourhood of the caustic has become much smoother than those in the model without a clump. The observed asymmetric feature along with the caustic centred at a bright clump has almost disappeared. Note that the remaining discontinuity at the edge of the caustic is due to the fact that the beam size (~ 0.1 arcsec) is much larger than the source size (~ 0.05 arcsec). Even in the cases where the lens model is perfectly correct, such a discontinuity is unavoidable.

In Fig. 16, we plot the difference between the model and observed images in the band 7 continuum data for each pixel in the image plane. To account for the beam smoothing effect, the pixel size is downgraded to 0.03 arcsec from 0.005 arcsec. We can see a prominent difference that consists of two bright clumps (in red colour) in the neighbourhood of Bq1 at $(x, y) \approx (-1.7, -0.3)$. The feature has become inconspicuous in the model with a clump. Moreover, the difference in the neighbourhood of Cq1 centred at $(x, y) \sim (-0.4, -1.5)$ has also become small in the model with a clump. These modifications are consistent with those observed in the source plane: the best-fitted model predicts too bright B and C images. In order to explain the demagnification of B image, we need to consider a perturbation by a negative density.

6 CONCLUSION AND DISCUSSION

In this paper, we have analysed the ALMA long baseline science verification data of the gravitational lens system SDP.81. We have fitted the positions of the brightest clumps in the source and a possible AGN component of the lensing galaxy in band 7 continuum image using a canonical lens model SIEES. Then, we have measured the ratio of fluxes in some apertures defined at the source plane where the lensed images are inversely mapped. We have found that the aperture fluxes of B and C images in the band 7 are demagnified by 10-20 percent in comparison with the A and D images with a significance at 2σ - 3σ level. We have observed an asymmetric feature along the caustic in the CO (8-7) line at

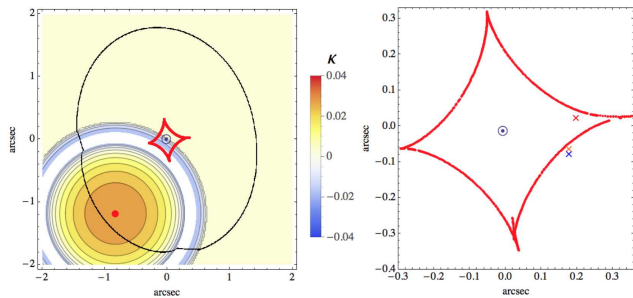


Figure 11. Convergence κ of a clump and critical curve (black) and caustic (red) for the best-fitted SIEES plus a clump model. The centre of the coordinates is at image G. In the left-hand panel, the red disk represents the centre of a compensated spherical clump in the line of sight. In the right-hand panel, the circled dot indicates the position of an SIE and crosses represent the positions of bright clumps in the source in the band 7 continuum image.

the 50th channel (rest-frame velocity 28.6 km s^{-1}) possibly due to astrometric shifts of the order of 0.01 arcsec by some perturbers. Based on a semi-analytic calculation, we find that the magnitudes of observed anomalous flux ratios and the astrometric shifts can be explained by dark structures on subgalactic scales in the line of sight. We have found that a spherical clump compensating in mass in the lens plane can explain the anomalous aperture flux ratios and an imprint of astrometric shifts. The redshift of the clump may be different from that of the primary lens. It can be directly measured if the astrometric shifts are measured with a good accuracy (Inoue & Chiba 2005a). Note that the perturbers may have a more complex structure that consists of haloes, filaments and voids (Inoue 2015).

One might be tempted to attribute the observed anomalous flux ratios to subhaloes or substructures in the lensing galaxy. However, we have found that a bright clump in image B with a positive parity is less magnified than the theoretical prediction in the band 7 continuum image. This feature cannot be explained by a presence of a positive density perturbation as it causes magnification of an unperturbed image. By subtracting a constant convergence from the fitted model and adding a constant shear, one can obtain negative surface density regions as well as positive ones without affecting the fluxes and positions of the fitted model due to the mass-sheet degeneracy. However, the amplitudes of convergence in such negative density regions are expected to be much smaller than those in positive density regions as the outskirts of infalling subhaloes are stripped and the spatial correlation between the subhaloes is reduced due to tidal force in the host halo.

Instead, one can consider a possibility that the anomaly is caused by the line-of-sight intergalactic structures. As is well known, the line-of-sight structures may consist of complex non-linear objects such as haloes, filaments, walls and voids. Therefore, the convergence perturbations consist of positive and negative density components which have a spatial correlation on scales of $\lesssim 10$ kpc. Although the amplitude of negative components is somewhat smaller than that of positive components, the probability of crossing with the photon path would be larger for negative components than

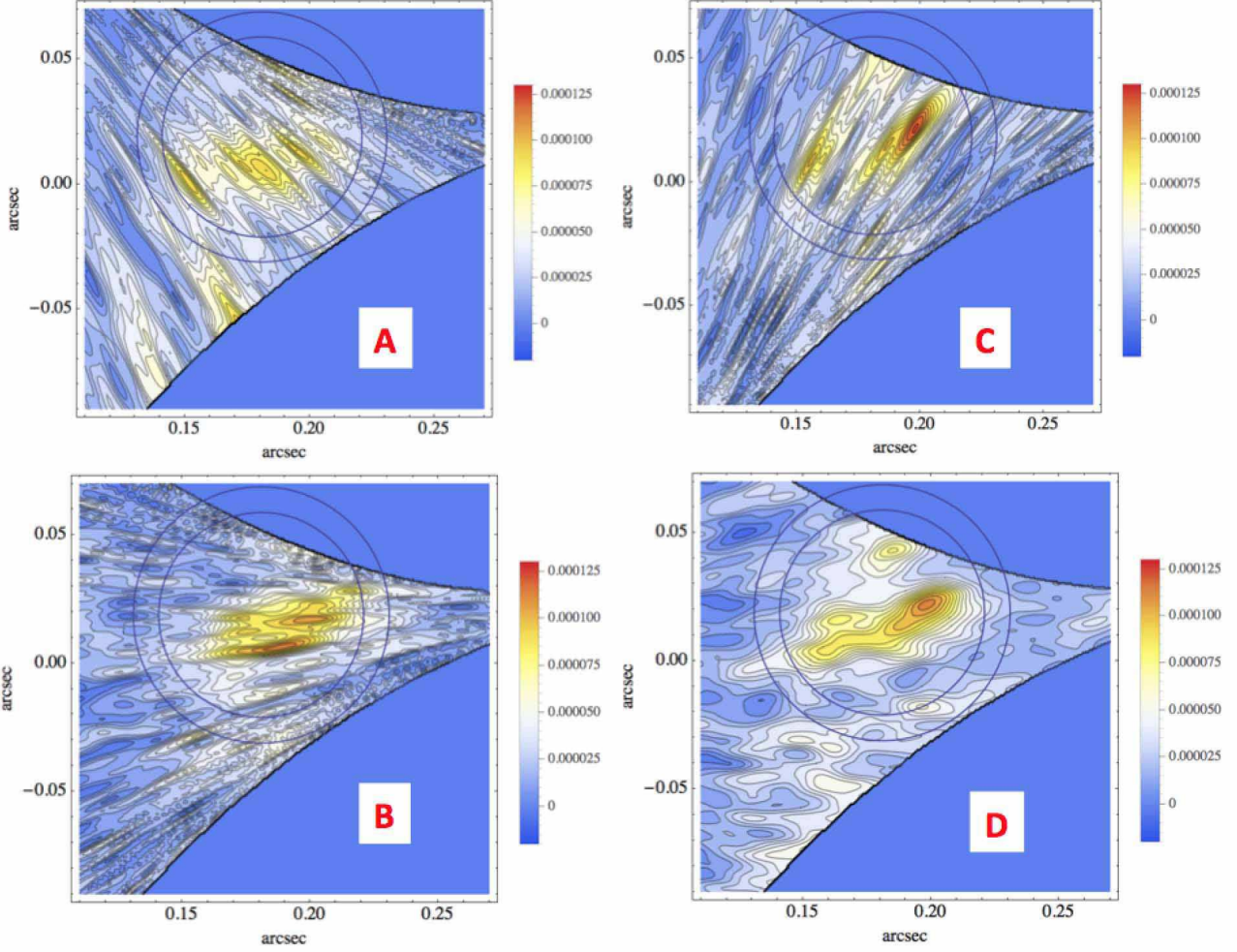


Figure 12. Inverted quadruple images of band 7 data using a best-fitted SIEES plus a homogeneous compensated clump model. The unit is Jy per beam. Blue circles denote apertures with radii 0.04 and 0.05 arcsec. The centre of the apertures is (0.1809, 0.01882) in the source plane.

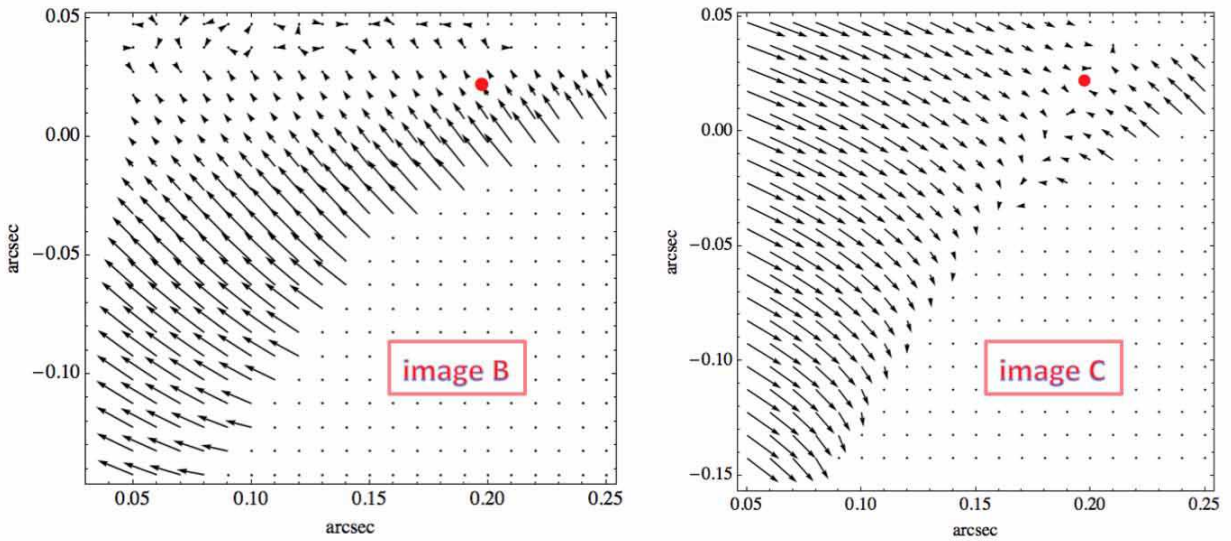


Figure 13. Astrometric shifts in the source plane for image B and C. The arrows represent the displacement of points due to a spherical compensated clump. Red discs (corresponding to the red disc in Fig. 11) show the position of the centre of the clump.

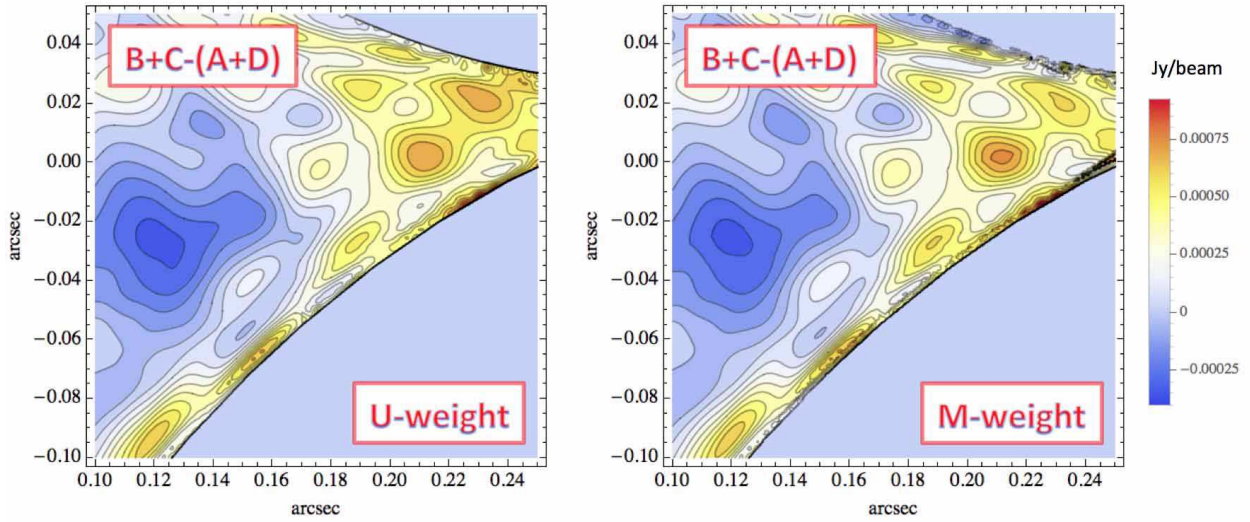


Figure 14. Difference between the source images reconstructed from B+C and A+D in the best-fitted model with a clump.

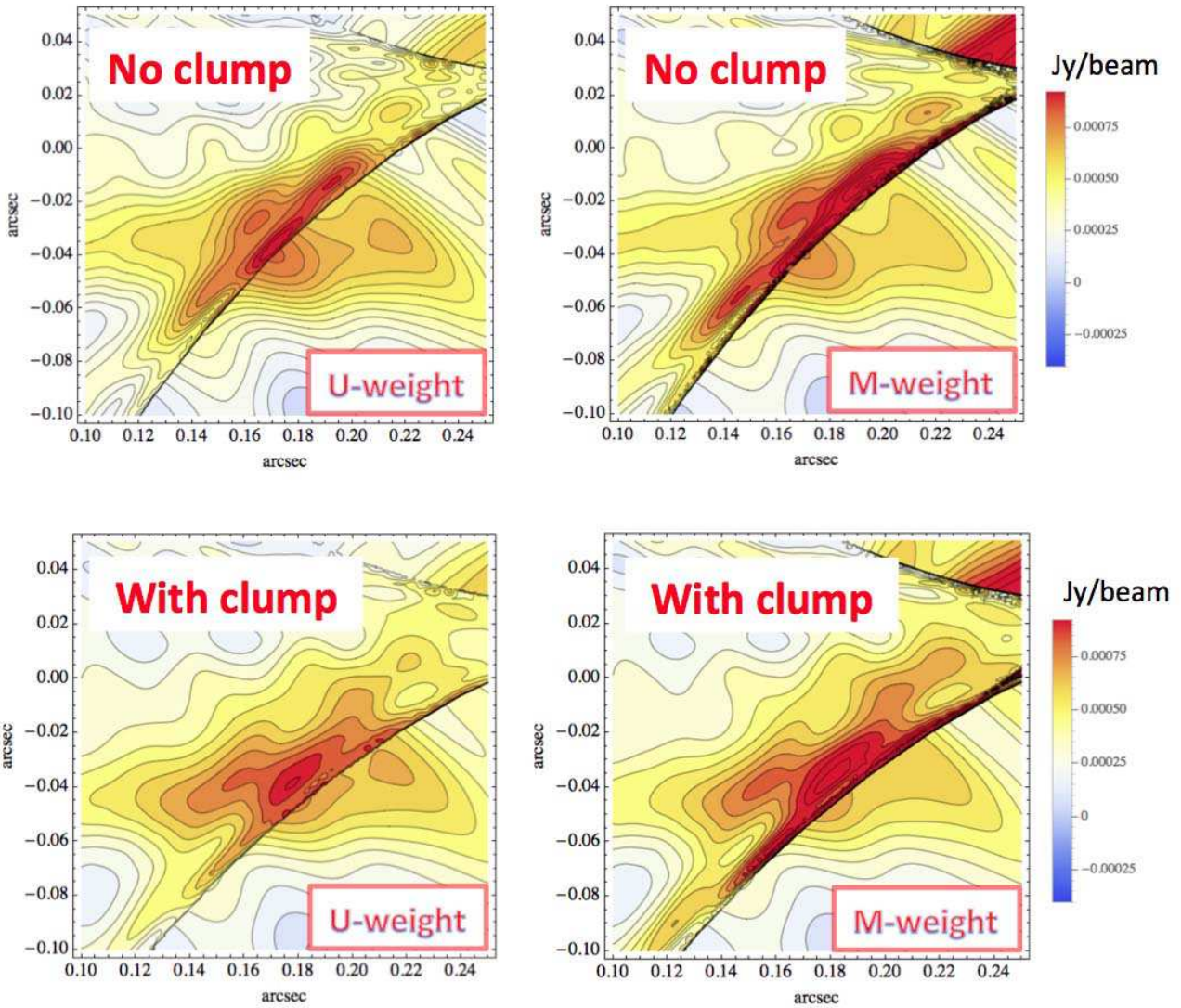


Figure 15. Reconstructed source images of the CO(8-7) Ch.50 map using the unperturbed (upper) and perturbed models (lower).

Table 5. Parameters of a Spherical Homogeneous Clump

(x_c, y_c)	b_c (arcsec)	\tilde{d}	θ_+ (arcsec)	$M(10^9 M_\odot/h)$
(-0.826,-1.184)	0.03	0.286	1.12	2.66

Table 6. Modification of Flux Ratios in Band 7

		aperture(arcsec)	$\eta(1\sigma)$	B/A	C/A	D/A	
best-fitted with a clump	0.06	0.043(0.039)	ratio	0.921	0.891	0.956	
			error	0.065	0.073	0.082	
			deviation	1.2	1.5	0.5	
	0.05	0.038(0.039)	ratio	0.935	0.910	0.983	
			error	0.062	0.073	0.078	
			deviation	1.1	1.2	0.2	
	0.04	0.035(0.036)	ratio	0.938	0.926	0.996	
			error	0.059	0.071	0.074	
			deviation	1.1	1.0	0.0	
	<hr/>						
			aperture(arcsec)	$\eta(1\sigma)$	B/A	C/A	D/A
	concordant with a clump	0.06	0.029(0.036)	ratio	0.937	0.919	0.980
error				0.071	0.067	0.078	
deviation				0.9	1.2	0.25	
0.05		0.030(0.037)	ratio	0.957	0.934	1.000	
			error	0.067	0.066	0.076	
			deviation	0.6	1.0	0.22	
0.04		0.034(0.036)	ratio	0.966	0.945	1.011	
			error	0.063	0.065	0.072	
			deviation	0.5	0.8	0.1	

positive ones. In order to find such perturbations, we need observations with a very good sensitivity and high resolution. ALMA is an ideal tool for carrying out such observations.

The canonical lens model that we have considered may have been too simple. Indeed, one can consider possibilities that the observed anomalies are due to simplification of the unperturbed model. For instance, inclusion of a core, a deviation from $\alpha = -2$ or a power law, higher multipoles, contribution from group galaxies or clusters may explain the anomalies. Indeed, increasing the number of model parameters would surely weaken the argument we have made. However, the observed anomalous feature in image B in the band 7 is localized in the neighbourhood of the brightest clumps. This suggests that the fluctuation scale of a possible perturbation is sufficiently smaller than the effective Einstein radius of the primary lens. Therefore, it is unlikely that modification of the potential of the unperturbed model on large scales leads to the local change of magnification. Changing the parameters of the best-fitted unperturbed model would not work unless one considers a non-smooth potential that is not physically motivated. In addition to the line-of-sight structures, subhaloes in the lens galaxy may also perturb the flux ratios to some extent. In order to probe which contribution is dominant over the other, observation of 21 cm absorption lines would be necessary as intergalactic structures may retain a large amount of neutral hydrogen gas.

We have not obtained an optimal solution for the perturbation of convergence and shear. The success of a simple toy model suggests that the perturbation consists of the both positive and negative density perturbations. The actual shape of these perturbation might be obtained by more sophisticated methods formulated either in the uv plane, image plane or source plane. It is also important to use all the available data at different frequencies. More realistic ray-tracing simulations beyond the Born approximation are necessary for understanding the nature of flux anomalies and astrometric shifts due to intergalactic structures. These issues should be addressed in our future work.

7 ACKNOWLEDGEMENTS

We thank Yoichi Tamura and Bunyo Hatsukade for useful discussions and comments. This work is supported in part by JSPS Grant-in-Aid for Scientific Research (B) (No. 25287062) ‘‘Probing the origin of primordial minihaloes via gravitational lensing phenomena’’, MEXT Grant-in-Aid for Scientific Research on Innovative Areas ‘‘Cosmic Acceleration’’ (No. 15H05889 for MC), and Ministry of Science and Technology (MoST) of Taiwan, MoST 103-2112-M-001-032-MY3. This paper makes use of the following ALMA data: ADS/JAO.ALMA#2011.0.00016.SV. ALMA is a partnership of ESO (representing its member states), NSF (USA) and NINS (Japan), together with NRC (Canada) and NSC and ASIAA (Taiwan), in cooperation with the Republic of

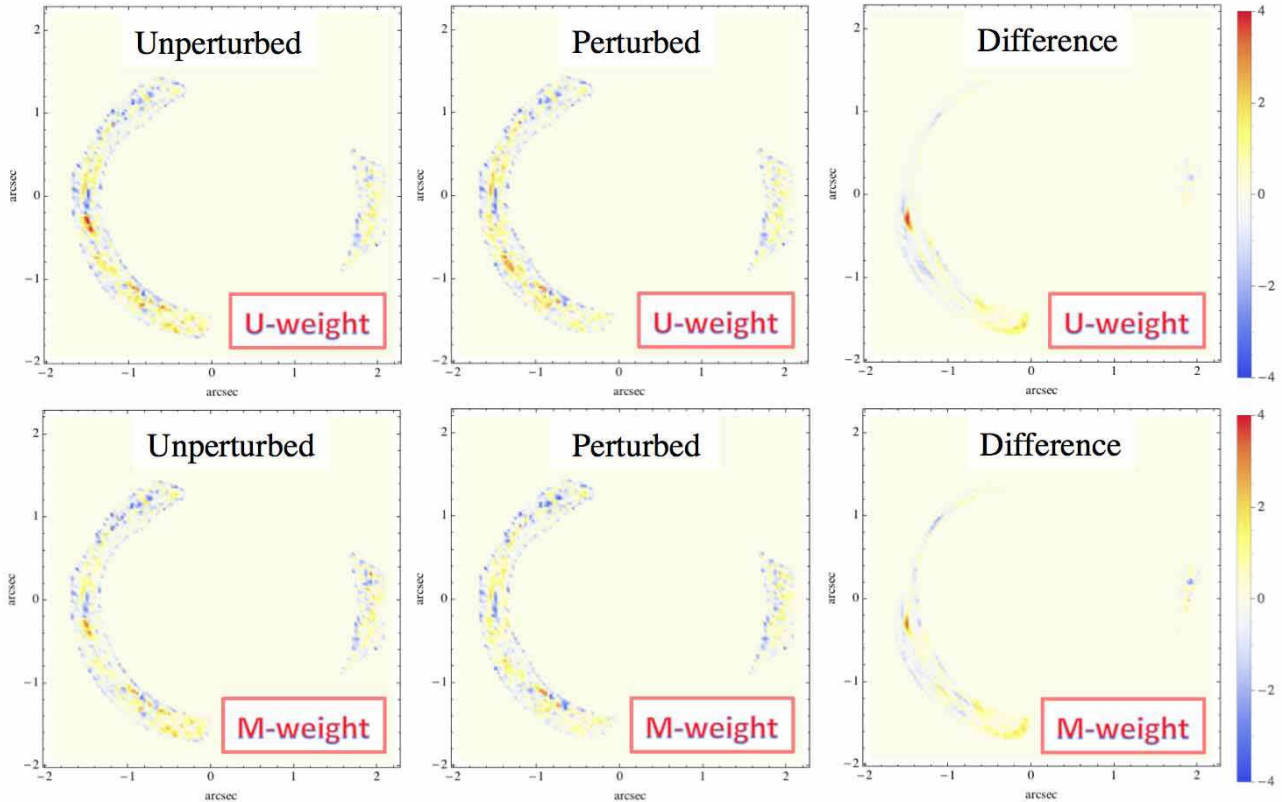


Figure 16. The surface brightness differences with the observed band 7 image in the image plane (the model minus data). The pixel size is 0.03 arcsec. The panels show the unperturbed (left) and perturbed (middle) best-fitted models and their differences (right). The unit is 1σ in one pixel.

Chile. The Joint ALMA Observatory is operated by ESO, AUI/NRAO and NAOJ.

REFERENCES

- ALMA Partnership et al., 2015a, *ApJ*, **808**, L1
ALMA Partnership et al., 2015b, *ApJ*, **808**, L4
Amendola L., Frieman J. A., Waga I., 1999, *MNRAS*, **309**, 465
Boylan-Kolchin M., Bullock J. S., Kaplinghat M., 2011, *MNRAS*, **415**, L40
Chen J., Kravtsov A. V., Keeton C. R., 2003, *ApJ*, **592**, 24
Chiba M., 2002, *ApJ*, **565**, 17
Chiba M., Minezaki T., Kashikawa N., Kataza H., Inoue K. T., 2005, *ApJ*, **627**, 53
Dalal N., Kochanek C. S., 2002, *ApJ*, **572**, 25
Dye S., et al., 2015, *MNRAS*, **452**, 2258
Hatsukade B., Tamura Y., Iono D., Matsuda Y., Hayashi M., Oguri M., 2015, *PASJ*, **67**, 93
Inoue K. T., 2015, *MNRAS*, **447**, 1452
Inoue K. T., Chiba M., 2005a, *ApJ*, **633**, 23
Inoue K. T., Chiba M., 2005b, *ApJ*, **634**, 77
Inoue K. T., Takahashi R., 2012, *MNRAS*, **426**, 2978
Inoue K. T., Takahashi R., Takahashi T., Ishiyama T., 2015, *MNRAS*, **448**, 2704
Keeton C. R., Kochanek C. S., Falco E. E., 1998, *ApJ*, **509**, 561
Keeton C. R., Gaudi B. S., Petters A. O., 2003, *ApJ*, **598**, 138
Klypin A., Kravtsov A. V., Valenzuela O., Prada F., 1999, *ApJ*, **522**, 82
Kormann R., Schneider P., Bartelmann M., 1994, *A&A*, **284**, 285
Mao S., Schneider P., 1998, *MNRAS*, **295**, 587
McKean J. P., et al., 2007, *MNRAS*, **378**, 109
McMullin J. P., Waters B., Schiebel D., Young W., Golap K., 2007, in Shaw R. A., Hill F., Bell D. J., eds, *Astronomical Society of the Pacific Conference Series Vol. 376, Astronomical Data Analysis Software and Systems XVI*. p. 127
Metcalf R. B., 2005, *ApJ*, **629**, 673
Metcalf R. B., Madau P., 2001, *ApJ*, **563**, 9
Metcalf R. B., Moustakas L. A., Bunker A. J., Parry I. R., 2004, *ApJ*, **607**, 43
Minezaki T., Chiba M., Kashikawa N., Inoue K. T., Kataza H., 2009, *ApJ*, **697**, 610
Moore B., Ghigna S., Governato F., Lake G., Quinn T., Stadel J., Tozzi P., 1999, *ApJ*, **524**, L19
More A., McKean J. P., More S., Porcas R. W., Koopmans L. V. E., Garrett M. A., 2009, *MNRAS*, **394**, 174
Navarro J. F., Frenk C. S., White S. D. M., 1996, *ApJ*, **462**, 563
Negrello M., et al., 2010, *Science*, **330**, 800
Negrello M., et al., 2014, *MNRAS*, **440**, 1999
Planck Collaboration et al., 2014, *A&A*, **571**, A1
Reid M. J., Honma M., 2014, *ARA&A*, **52**, 339
Reid M. J., Schneps M. H., Moran J. M., Gwinn C. R., Genzel R., Downes D., Roennaeng B., 1988, *ApJ*, **330**, 809
Rybak M., McKean J. P., Vegetti S., Andreani P., White S. D. M., 2015a, *MNRAS*, **451**, L40
Rybak M., Vegetti S., McKean J. P., Andreani P., White S. D. M., 2015b, *MNRAS*, **453**, L26
Simon J. D., Bolatto A. D., Leroy A., Blitz L., Gates E. L., 2005, *ApJ*, **621**, 757
Simpson J. M., et al., 2014, *ApJ*, **788**, 125
Sugai H., Kawai A., Shimono A., Hattori T., Kosugi G., Kashikawa N., Inoue K. T., Chiba M., 2007, *ApJ*, **660**, 1016

- Swaters R. A., Madore B. F., van den Bosch F. C., Balcells M., 2003, [ApJ](#), **583**, 732
- Takahashi R., Inoue K. T., 2014, [MNRAS](#), **440**, 870
- Tamura Y., Oguri M., Iono D., Hatsukade B., Matsuda Y., Hayashi M., 2015, [PASJ](#), **67**, 72
- Vegetti S., Lagattuta D. J., McKean J. P., Auger M. W., Fassnacht C. D., Koopmans L. V. E., 2012, [Nature](#), **481**, 341
- Wang J., Frenk C. S., Navarro J. F., Gao L., Sawala T., 2012, [MNRAS](#), **424**, 2715
- Wong K. C., Suyu S. H., Matsushita S., 2015, [ApJ](#), **811**, 115
- Xu D. D., et al., 2009, [MNRAS](#), **398**, 1235
- Xu D. D., Mao S., Cooper A. P., Wang J., Gao L., Frenk C. S., Springel V., 2010, [MNRAS](#), **408**, 1721
- Xu D. D., Mao S., Cooper A. P., Gao L., Frenk C. S., Angulo R. E., Helly J., 2012, [MNRAS](#), **421**, 2553